Journal of Alloys and Compounds 897 (2022) 162820

Contents lists available at ScienceDirect

Journal of Alloys and Compounds

journal homepage: www.elsevier.com/locate/jalcom

Realization of neutral white light emission in $CaMoO_4$:4Dy^{3+} phosphor via Sm^{3+}co-doping

Prashant Dixit[a], Vaibhav Chauhan[a], S.B. Rai[b], Praveen C. Pandey[a,*]

[a] Department of Physics, Indian Institute of Technology (Banaras Hindu University), Varanasi, U.P. 221005, India
[b] Department of Physics, Banaras Hindu University, Varanasi, U.P. 221005, India

ARTICLE INFO

Article history:
Received 13 August 2021
Received in revised form 26 October 2021
Accepted 15 November 2021
Available online 23 November 2021

Keywords:
$CaMoO_4$
Dy^{3+} ion
Sm^{3+} ion
Photoluminescence
Energy transfer

ABSTRACT

In this paper, Dy^{3+}/Sm^{3+} co-doped $CaMoO_4$ compounds were synthesized successfully via the auto-combustion method. The tetragonal crystal structure of the phosphors is confirmed by structural study. The vibrational modes are examined by infrared spectroscopy. It has been observed that 4% Dy^{3+} doped $CaMoO_4$ phosphor shows maximum luminescence intensity. Further, Sm^{3+} ions are co-doped in 4% Dy^{3+} doped $CaMoO_4$ for improving their luminescence properties. The Photoluminescence study illustrates energy transfer between $[MoO_4]^{-2}$ groups and Dy^{3+}/Sm^{3+} ions, under 296 nm excitation. The Dy^{3+} doped $CaMoO_4$ phosphors emit two sharp peaks at 484 nm ($^4F_{9/2}\rightarrow{}^6H_{15/2}$) and 574 nm ($^4F_{9/2}\rightarrow{}^6H_{13/2}$). Further, with Sm^{3+} co-doping in 4% Dy^{3+} doped $CaMoO_4$ phosphor, another distinctive emission peak is observed at 647 nm, which is attributed to $^4G_{5/2}\rightarrow{}^6H_{9/2}$ electric dipole transition of Sm^{3+} ion. The Dy^{3+}/Sm^{3+} co-doped $CaMoO_4$ phosphor gives overall white light emission. For 3% Sm^{3+} co-doped $CaMoO_4$:4Dy^{3+} phosphor, white light is obtained with the CCT value of 4439 K. Hence, the prepared phosphor might be used in white lighting diode applications.

© 2021 Elsevier B.V. All rights reserved.

1. Introduction

In the last decade, the white light-emitting diodes (w-LEDs) have been preferred over conventional light sources owing to their environmental amiableness, enhanced optical power, and electrical power saving capacity [1-3]. Most commercial w-LEDs nowadays use Ce^{3+}:YAG as the yellow phosphor deposited on the InGaN blue chip to produce white light [4-6]. The white light generated by such a device constitutes cold-white light with high correlated color temperature (more than 5000 K), which is because of the shortage of red color components [7-9]. Some researchers have proposed new w-LEDs that emit white light using an ultraviolet (UV) LED chip and tricolor (RGB) phosphors. However, this technique has many drawbacks in terms of color ratio adjustment, re-absorption of color, and radiant efficiency [10,11]. Hence, a single-color ingredient phosphor is desired that emits good white light near UV absorption [12-14].

Scientists have studied various phosphors as host matrix for developing white-light emitting phosphors. Many studied phosphors such as Ca_2SiO_4 [15], CaF_2 [16], $SrWO_4$ [17], $CaSrAl_2SiO_7$ [18], have various disadvantages such as complex synthesis process which imposes limitations on their large scale production, low thermal and chemical stability. Therefore, the search to develop chemically and thermally stable phosphors which can be developed by cost-efficient and environmental friendly technique have gained importance. The molybdates such as $CaMoO_4$ have attracted interested of research fraternity owing to its extraordinary qualities. The $CaMoO_4$ has a tetragonal crystal structure with space group $I4_1/a$. $CaMoO_4$ is a self-activated phosphor that emits broadband emission from blue to the yellow visible region centered at a green light when exposed to near UV radiation [19]. In recent years, $CaMoO_4$ is being investigated as a viable phosphor because of its prominent applications in different fields, as photoluminescence [20], photocatalysis [21], white light-emitting diodes [22], optical fibers [23], scintillators [24], microwave applications [25], biomedical applications [26], and laser materials [27], etc. The advantage of $CaMoO_4$ over other phosphors is that, $CaMoO_4$ is thermally and chemically stable and has a stable tetragonal crystal structure. Other advantages of $CaMoO_4$ include high melting point (1435–1480 °C), average effective decay time (14 ms), and non-hygroscopic [28]. The $CaMoO_4$ phosphor is synthesized via different synthesis processes, such as hydrothermal/solvothermal [29,30], sol-gel [31,32], solid-state technique [33], and one-step spray pyrolysis [34]. Among various synthesis processes, the urea-based auto-combustion process is advantageous over others owing to its cost-effectiveness.

The emitting color can be tuned via doping of various rare-earth elements in $CaMoO_4$ phosphor because of the various arrangements

* Corresponding author.
E-mail address: pcpandey.app@iitbhu.ac.in (P.C. Pandey).

https://doi.org/10.1016/j.jallcom.2021.162820
0925-8388/© 2021 Elsevier B.V. All rights reserved.

of the 4 f electrons.The rare-earth elements have discrete energy levels because of the various arrangement of the 4 f electrons. Due to transitions of the 4 f electrons among the different energy levels, a variety of fluorescence spectra can be realized. Therefore, most of the rare-earth-doped phosphors have been utilized for various applications [35,36]. The Dy^{3+} doped $CaMoO_4$ phosphor has two intense emission peaks that are observed at 488 nm and 574 nm, which corresponds to the $^4F_{9/2}\rightarrow{}^6H_{15/2}$ and $^4F_{9/2}\rightarrow{}^6H_{13/2}$ transitions of the Dy^{3+} ions, respectively [22]. Under the $CaMoO_4$ excitation, emission spectra of Dy^{3+} doped $CaMoO_4$ illustrate that energy transfer successfully occurs between $[MoO_4]^{-2}$ to Dy^{3+} energy level [22]. Therefore, Dy^{3+} doped $CaMoO_4$ has been used in various applications [37,38]. The efficiency of both Dy^{3+} emission peaks has a significant impact on the device efficiency of these materials. The overall white emission can be realized by adjusting the intensity of blue and yellow emission of Dy^{3+} ion, but such white light lacks a red component. Earlier reported Dy^{3+} doped phosphors such as $Na_3ScSi_2O_7$:Dy^{3+} [2], $CaMoO_4$:Dy^{3+} [22], $Na_3MgZr(PO_4)_3$:Dy^{3+} [39], $Ba_3La(PO_4)_3$:Dy^{3+} [40], and $Ba_3Y(PO_4)_3$:Dy^{3+} [41] have studied the luminescence property of Dy^{3+} ion. The lack of the red component in the overall emission of the Dy^{3+} doped phosphors limits their use in commercial w-LEDs. Recently, there are some reports on Dy^{3+}/Sm^{3+} co-doping in other host materials such as $Na_5Y_9F_{32}$, BaY_2ZnO_5, and $Ca_2La_8(SiO_4)_6O_2$ for developing white light source. But these phosphors have various drawbacks such as use of high temperature solid state method, and weak self-luminescence [42-44].

In this paper, we have co-doped red-emitting Sm^{3+} ions in 4% Dy^{3+} doped $CaMoO_4$ phosphor for removing the earlier discussed drawbacks as they have a forceful red emission peak at 647 nm ($^4G_{5/2}\rightarrow{}^6H_{9/2}$). The red emission of Sm^{3+} ions in the $CaMoO_4$:4Dy^{3+} shifts the overall emission of Dy^{3+} doped $CaMoO_4$ phosphor from bluish white light to neutral white light [45]. The calculated CCT decreases continuously with Sm^{3+} co-doping in 4%Dy^{3+}:$CaMoO_4$. Thus, by adjusting the concentration of the Dy^{3+} and Sm^{3+}ions in $CaMoO_4$, we can achieve excellent white light emissions with CCT < 5000 K. The prepared Sm^{3+}/Dy^{3+} co-doped $CaMoO_4$ phosphors might be used as white light-emitting diode devices.

2. Synthesis and characterizations

2.1. Synthesis of Dy^{3+} doped, Sm^{3+} doped, and Sm^{3+} co-doped $CaMoO_4$:4Dy^{3+} phosphors

We have prepared pure phase $CaMoO_4$, x%(x = 2, 3, 4 & 5) Dy^{3+} doped $CaMoO_4$, y%(y = 2, 3, & 4) Sm^{3+} doped $CaMoO_4$ and z%(z = 1, 2, 3 & 4) Sm^{3+} co-doped 4%Dy^{3+}:$CaMoO_4$ samples via facile auto-combustion method and are specified with code names CMO, D2, D3, D4, D5, Sm2, Sm3, Sm4, S1, S2, S3 & S4, respectively. The starting materials for synthesis were $CaCO_3$, (Alfa Aesar, 99.5%), $(NH_4)_6Mo_7O_{24}$ * 4 H_2O (Alfa Aesar, 99%), $Dy(COOCH_3)_3$ * 4 H_2O (Sigma-Aldrich, 99.9%), and $Sm(COOCH_3)_3$ *xH_2O (Sigma-Aldrich, 99.9%). Briefly, for the preparation of the S3 sample, the required amounts of $CaCO_3$, $Dy(COOCH_3)_3$ * 4 H_2O, and $Sm(COOCH_3)_3$ *xH_2O were taken in a beaker, and $HNO_3$was added drop by drop for 2–3 h. After that, we obtained a transparent gel solution of metal nitrates. It is heated continuously to remove excess acid from the utility. After that, a required amount of $(NH_4)_6Mo_7O_{24}$.4 H_2O was taken in another beaker with distilled water and placed under constant stirring for 2 h at room temperature. A required amount of urea is added to the solution to facilitate the process of auto-combustion, and this solution is stirred at a constant rate for the next 1 h to make a homogeneous solution. This homogenous solution was mixed with the above metal nitrate solution at 120 °C. The auto-combustion was facilitated by keeping the final solution in an oven preset at 250 °C for 4 h. The resulting powder sample obtained after combustion was annealed at 1000 °C for 4 h in a closed furnace. A similar synthesis procedure has been performed for all samples.

2.2. Characterizations

The x-ray diffraction (XRD) patterns of all synthesized phosphors have been obtained over the 2θ range of 10° to 80° from the Rigaku-Mini Flex II DESKTOP powder X-ray diffractometer. The X-ray photoelectron spectroscopy (XPS) data is obtained from Thermo Fisher Scientific, K-alpha X-ray photoelectron spectrometer to verify the oxidation states of various elements present in the sample. The particle size images have been observed via an EVO-Scanning Electron Microscope (MA15/18). The FTIR spectrums have been obtained by JASCO FT/IR 4600. The UV-Vis absorption spectrum of all prepared samples have been observed using JASCO V770 UV-Vis-NIR spectrophotometer. The Photoluminescence (excitation and emission) spectrums of all the prepared samples have been obtained using a Horiba Fluorolog-3 spectrophotometer.

3. Results and analysis

3.1. XRD study

The Rietveld refined XRD pattern of CMO, D4, and S3 is demonstrated in Fig. 1. The XRD pattern corroborates the tetragonal crystal structure of all the prepared phosphors. Some of the observed diffraction peaks such as (101), (112), (004), (200), (212), (204), (220), (116), (312), (224) have been indexed with space group symmetry $I4_1/a$ (JCPDS file number 85–1267 (a=b=5.223, c=11.429)) [46]. The structure of $CaMoO_4$ is a 3D framework formed by dodecahedral [CaO_8] clouds and tetrahedral [MoO_4] clouds attached via common vertices Ca–O–Mo [47]. The crystal structure of the prepared phosphor is depicted in Fig. 1(d). The ionic radius of Dy^{3+} (91.2 pm) and Sm^{3+} (108 pm) ions are closer to the ionic radius of Ca^{2+}ion (100 pm) [48]. Therefore, it is expected that Dy^{3+} and Sm^{3+} ions must have been substituted in the Ca^{2+} ion sites. The volume of the unit cell and the lattice parameters of all the prepared samples have been obtained by Rietveld refinement using FULLPROF software [49]. The obtained lattice parameters and cell volume of prepared phosphors are shown in Fig. 2(a) and tabulated in Table 1. For the host phosphor CMO, the cell volume is 312.315 $Å^3$, and the lattice parameters are a=b= 5.226 Å, c= 11.435 Å, as listed in Table 1. The unit cell volume decreases after Dy^{3+} doping in CMO because the ionic radius of the Dy^{3+} ion (91.2 pm) is less than that of the Ca^{2+} ion (100 pm), the variation in unit cell volume again confirms that Dy^{3+} ions are substituted in Ca^{2+} ion sites. The lattice parameter and the unit cell volume increase with the increasing co-doping concentration of Sm^{3+} because the ionic radii of Sm^{3+} (108 pm) are higher than the Ca^{2+} ion (100 pm). We have observed that the unit cell volume for a low concentration of Sm^{3+} (for S1 sample) is less than D4 phosphor, which may be due to increased diffusion and migration between different ions [45]. After further increasing the concentration of Sm^{3+} ion, it occupies the substitutional position, causing an increase in the volume of the unit cell and corresponding transformations in lattice parameters.

We used the Williamson-Hall (W–H) method with the following formula for the calculation of crystallite size (d) and microstrain (ε) in the lattice [50];

$$\boldsymbol{\beta\, sin\theta = 4\varepsilon\, cos\theta + \left(\frac{K\lambda}{d}\right)}$$

Where β is the calculated full width at half maxima (FWHM in radians) computed by deducting instrumental peak broadening ($\beta_{instrument}$) corresponding to the diffraction peak angle θ in the XRD pattern, λ = 1.54 Å is the wavelength of X-ray corresponding to Cu Kα radiation used in the XRD, and K is a shape factor (K~0.9). The graph of W-H expression demonstrates a linear equation $\boldsymbol{y = mx + c}$ in the plot of $\beta sin\theta$ versus cos θ. The slope of this linear equation gives the calculated value of the lattice strain (ε), and the intercept of this linear equation gives the crystallite size (d) of the samples. The

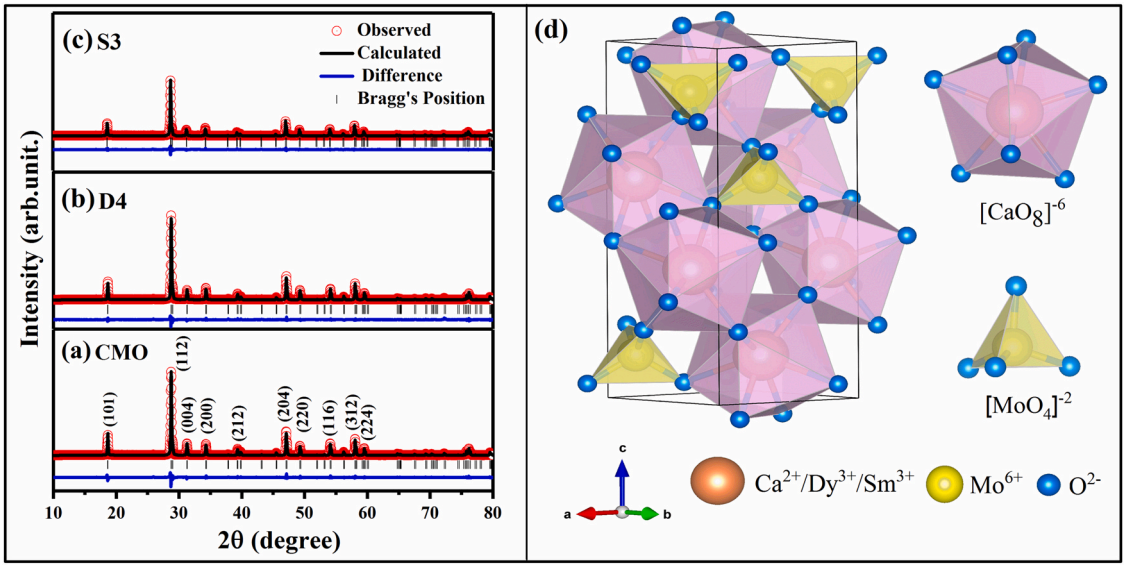

Fig. 1. Rietveld refinement graph for (a) CMO, (b) D4, (c) S3 and (d) Crystal structure of prepared phosphors.

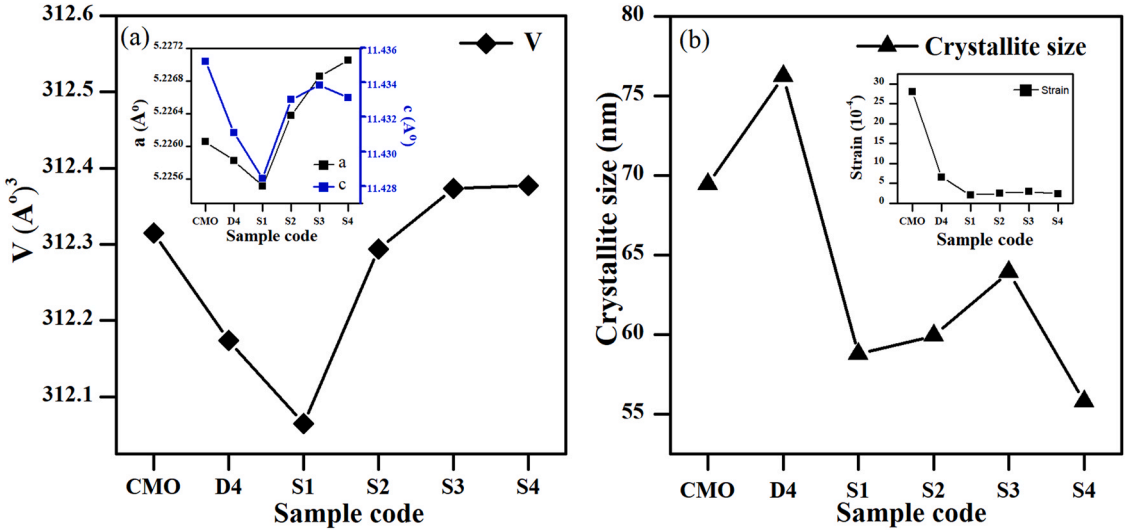

Fig. 2. (a) Variation of volume for Sm^{3+}/Dy^{3+}co-doped $CaMoO_4$. Inset shows variation of lattice parameters (b) Variation of crystallite size for Sm^{3+}/Dy^{3+}co-doped $CaMoO_4$. Inset shows variation of lattice strain.

variation in crystallite size and lattice strain is shown in Fig. 2(b) and is tabulated in Table 1. For $CaMoO_4$ phosphor, the crystallite size is 69 nm, and the microstrain is 0.0028. For Dy^{3+} doped samples, the crystallite size increases, as shown in Fig. 2(b). The increased crystallite size indicates more crystallinity of the sample. 4% Dy^{3+} doped $CaMoO_4$ sample has the maximum crystallite size (76 nm), which illustrates the high crystalline nature of the D4 sample. The crystallite size decreases upon co-doping of Sm^{3+} in $CaMoO_4$:4%Dy^{3+}, as shown in Fig. 2(b), but with a further increase in the concentration of Sm^{3+} ion, the crystallite size increases and is maximum (64 nm) for the S3 sample. The increase in the crystallinity of the phosphors results in reducing the density of the grain boundaries. The decrease in grain boundaries helps in improving the luminescence of the phosphor as grain boundaries result in light absorption with is produced within the crystal lattice [51].

The lattice strain is a measure of the lattice distortions present in the crystal, which arises due to crystal defects. The calculated value of lattice strain for $CaMoO_4$ phosphor is 0.0028 and it reduces with increasing the Dy^{3+} doping percentage. After Sm^{3+} co-doping, the lattice strain is further reduced. The lattice strain remains almost the same as the doping concentration of Sm^{3+} is increased, as presented in the inset of Fig. 2(b). The reduced lattice strain indicates that crystal defects decrease in the sample, which helps in emission intensity enhancement [52].

Table 1
Refinement parameters, crystallite size and strain values for (a) CMO, (b) D4, and (c) S3.

Parameters	CMO	D4	S3
Ca (x, y, z)	(0, 1/4, 5/8)	(0, 1/4, 5/8)	(0, 1/4, 5/8)
Mo (x, y, z)	(0, ¼, 1/8)	(0, ¼, 1/8)	(0, ¼, 1/8)
O (x, y, z)	(0.1480, 0.0004, 0.2086)	(0.1479, −0.0016, 0.2093)	(0.1474, −0.0008, 0.2088)
Angles (α, β, γ)	(90, 90, 90)	(90, 90, 90)	(90, 90, 90)
Lattice parameters in Å	a=b= 5.2260, c= 11.4352	a=b= 5.2258, c= 11.4310	a=b= 5.2268, c= 11.4331
Unit cell volume in Å^3	312.3148	312.1690	312.3458
χ^2	3.3	2.9	4.5
Crystallite size (d) nm	69.43	76.23	63.90
Lattice Strain (10^{-4})	28	6.63	3.05

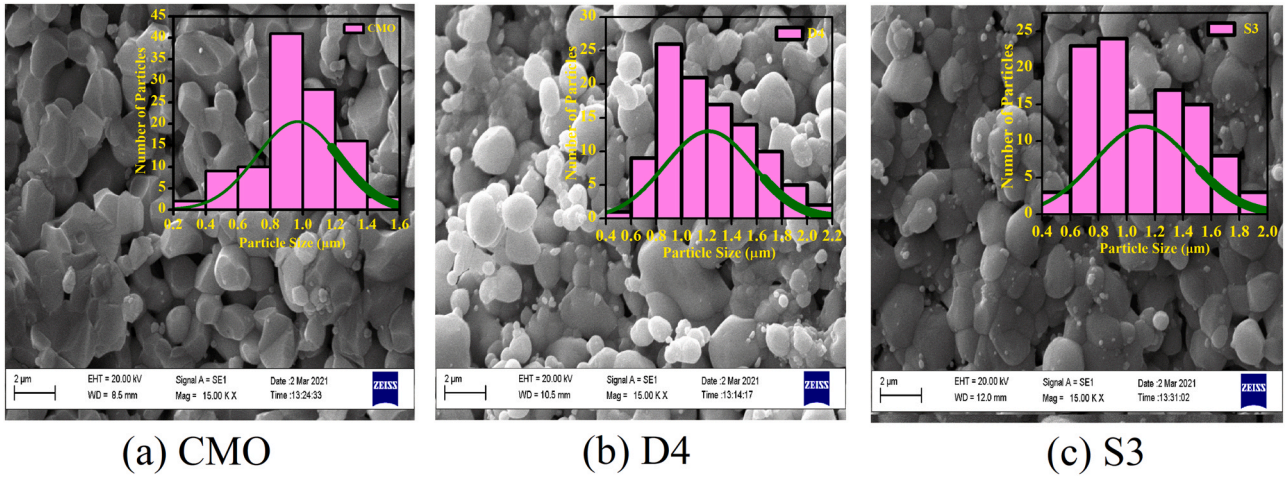

Fig. 3. SEM image of (a) CMO, (b) D4, and (c) S3.

3.2. Scanning electron micrograph image analysis

The SEM images of CMO, D4, and S3 samples calcined at 1000 °C are depicted in Fig. 3. The SEM images show the agglomerated spherical shape of particles for CMO, D4, and S3 samples. The average particle size of CMO phosphor is 0.97 μm. Agglomeration of particles occurs due to the creation of covalent or metallic bonds, which are affected by doping elements. The average particle size increases after Dy^{3+}/Sm^{3+} doping, and the value of average particle size for D4 and S3 samples are 1.21 μm and 1.12 μm, respectively.

3.3. XPS analysis

The oxidation states of elements present in the S3 phosphor have been investigated via the XPS technique. The survey scan of S3 is depicted in Fig. 4(a). The significant peaks of calcium, molybdenum, oxygen, dysprosium, and samarium are explicitly visible and labeled in the survey scan. The XPS binding energy spectrum of Ca2p, Mo3d, O1s, Dy3d, and Sm3d positions for the S3 sample are shown in Fig. 4(b) to 4(f) and tabulated in Table 2. Fig. 4(b) shows two bands centered at ~347.28 eV and ~350.78 eV, which are ascribed to $^2p_{3/2}$ and $^2p_{1/2}$ bound states of Ca^{2+} ion [53,54], respectively. The XPS spectra of Ca^{2+} ions confirm the +2 oxidation state of calcium in the S3 phosphor. Fig. 4(c) shows XPS scan for the Mo 3d core level and the observed peaks are at ~232.88 eV and ~235.98 eV attributed to the binding energy of Mo^{6+} $^3d_{5/2}$ and Mo^{6+} $^3d_{3/2}$ [53,54], respectively, which manifests +6 oxidation state of molybdenum in the S3. Fig. 4(d) shows an asymmetric nature in XPS scan for O1s level, which decomposes into two symmetric peaks centered at ~530 eV and ~531.08 eV [53,54]. This deconvolution of peaks arises from the bonding of oxygen with different elements in the S3 phosphor. The variation in the height of the O1s peak is due to the different electronegativity of the elements present in the sample [55]. The XPS scans of Dy^{3+} and Sm^{3+} ions are presented in Fig. 4(e) and Fig. 4(f),

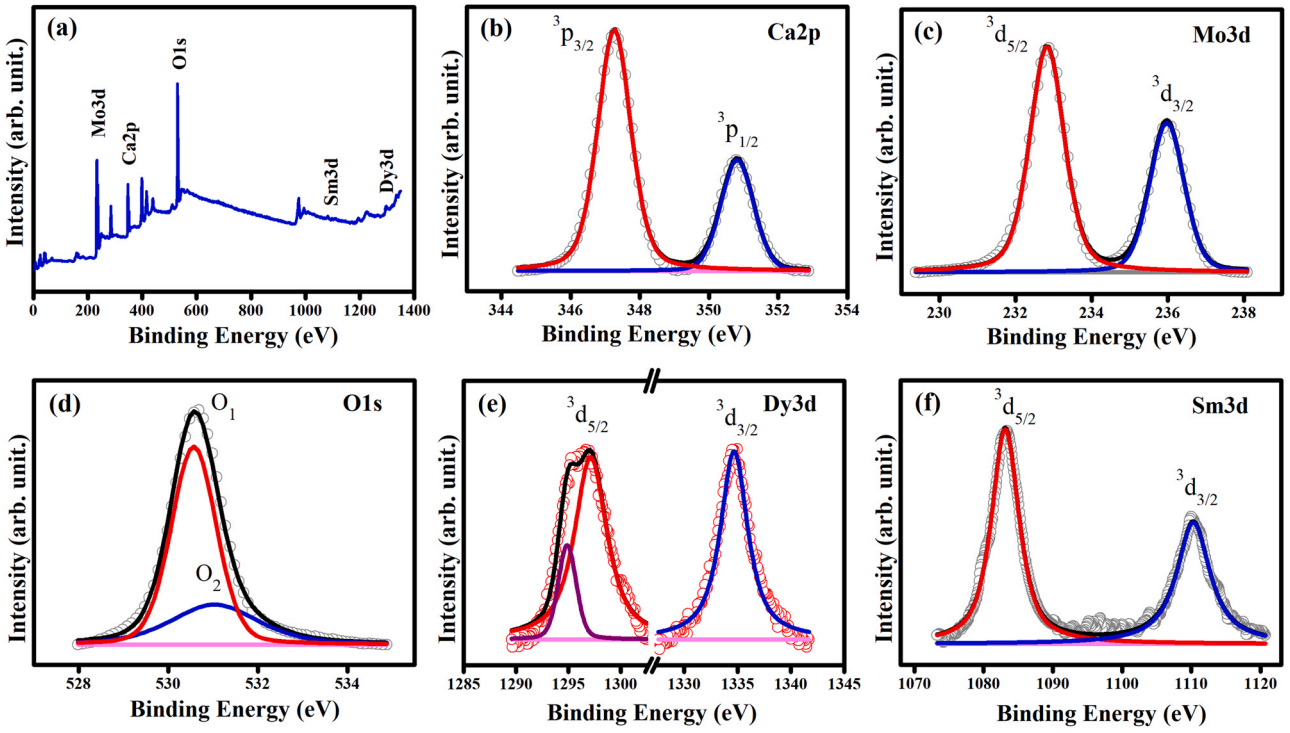

Fig. 4. (a) XPS survey for S3. High resolution XPS scan of (b) Ca 2p, (c) Mo 3d, (d) O 1 s, (e) Dy 3d, and (f) Sm 3d for S3 sample.

Table 2
Binding energies of all the elements in S3 sample.

Elements	State	B.E. (eV)
Ca 2p	Ca^{+2} $2p_{3/2}$	347.28
	Ca^{+2} $2p_{1/2}$	350.78
Mo 3d	Mo^{+6} $3d_{5/2}$	232.88
	Mo^{+6} $3d_{3/2}$	235.98
O 1 s	O_1^{-2}	530.0
	O_2^{-2}	531.08
Dy 3d	Dy^{+3} $3d_{5/2}$	1295
		1297.08
	Dy^{+3} $3d_{3/2}$	1334.58
Sm 3d	Sm^{+3} $3d_{5/2}$	1083.08
	Sm^{+3} $3d_{3/2}$	1110.28

respectively. The two prominent bands are observed in Fig. 4(e), one of them is the asymmetric band that corresponds to the binding energy of Dy3d $^3d_{5/2}$, which deconvolute into two symmetrical peaks centered at ~1295 eV, and ~1297.08 eV. The deconvolution of the peaks may be due to spin-orbit splitting in the Dy3d core level [56,57]. The second band centered at ~1334.58 eV is symmetrical, which correlates to the binding energy of $^3d_{3/2}$ of Dy3d [56,57]. Fig. 4(f) depicts the XPS scan of Sm3d core level with two bands centered at ~1083.08 eV and ~1110.28 eV which are attributed to Sm3d $^3d_{5/2}$ and Sm3d $^3d_{3/2}$, respectively [58]. The XPS scans manifest that dysprosium and samarium ions are in a +3 oxidation state.

3.4. FTIR analysis

The FTIR spectra of CMO, D4, and S3 samples have been recorded within the wave number range of 400 cm^{-1} to 4000 cm^{-1}. A total of 26 vibrational modes are present in the $CaMoO_4$ crystal structure, which is expressed by the following equation [59],

$$\Gamma = 3A_g + 5A_u + 5B_g + 3B_u + 5E_g + 5E_u$$

Out of 26 vibrational modes, 8 modes ($4A_u + 4E_u$) are infrared active and 13 modes ($3A_g + 5B_g + 5E_g$) are Raman active [54]. The observed FTIR vibrational modes in CMO, D4, and S3 samples are depicted in Fig. 5(a) and are tabulated in Table 3. The two transmission depths are detected in the fingerprint region from 400 cm^{-1} to 1400 cm^{-1}. One of them has an intense depth, which is centered at ~769.45 cm^{-1} and it corresponds to A_u and E_u modes due to antisymmetric bond stretching of O—Mo—O of $[MoO_4]^{-2}$ tetrahedron. A second band is observed at ~429.8 cm^{-1} which corresponds to A_u mode arising due to bending of Mo–O bond [20,54]. The observed vibrational bands confirm the tetragonal structure of all samples. An additional peak is detected at ~2360 cm^{-1}, corresponding to the asymmetric stretching vibration of CO_2 molecule [20,54].

Table 3
FTIR vibrational bands of CMO, D4, and S3 samples.

Sample Code Name	Vibrational Band (cm-1)		
	Bending of Mo-O bond	Stretching of O-Mo-O	Stretching of O=C=O
CMO	429.8	769.45	2360
D4	429.8	769.45	2361.2
S3	429.8	769.45	2358.51

3.5. UV-visible spectroscopy

The absorption spectrums of all phosphors have been recorded in the 200–1000 nm wavelength range. The absorption band obtained for the CMO sample is centered at 300 nm and is shown in Fig. 5(b). This absorption band results from charge transfer from O^{2-} to Mo^{6+} [60]. The absorption band peak shifts at 310 nm after the doping of Dy^{3+}/Sm^{3+} ions. The width of the absorption band increases for the Dy^{3+}/Sm^{3+} doped phosphors, which is due to the overlapping of charge transfer bands (CTBs) of O^{2-} to Mo^{6+}, O^{2-} to Dy^{3+} and O^{2-} to Sm^{3+}. Some peaks at 762 nm, 810 nm, and 912 nm are observed in the Dy^{3+} doped $CaMoO_4$ samples, which are ascribed to the transition from $^6H_{15/2}$ to ^6F_J (J=3/2, 5/2, and 7/2) levels of Dy^{3+} ion, respectively. The peaks are in good agreement with the earlier reports [61]. After co-doping of Sm^{3+} ions in the D4 sample, some other peaks are observed at 404 nm and 480 nm which are attributed to $^6H_{5/2}\rightarrow{}^4F_{7/2}$ and $^6H_{5/2}\rightarrow{}^4I_{9/2}$, $^4I_{11/2}$ & $^4I_{13/2}$ transitions of Sm^{3+} ions, respectively [62].

The optical bandgap (E_g) for prepared samples have been evaluated using the "Wood and Tauc" expression as given below;

$$\alpha h\nu = C(h\nu - E_g)^n$$

Where α is an absorption coefficient, $h\nu$ is the energy of an incident photon, and C is a constant [62]. The nature of the bandgap determines the value of the exponent n. $CaMoO_4$ has an allowed direct bandgap, so the value of n is taken to be 1/2 [63]. The intercept of the x-axis of the $(\alpha h\nu)^2$ versus $h\nu$ plot gives the approximate value of the bandgap. The Tauc plot is depicted in the inset of Fig. 5(b). The evaluated bandgap of the $CaMoO_4$ is 3.83 eV. The bandgap for Dy^{3+} doped phosphor reduces up to 3.35 eV. The redshift in the bandgap occurs due to the creation of intermediate energy levels of Dy^{3+} in the bandgap [63]. The Sm^{3+} co-doping into 4% Dy^{3+} doped $CaMoO_4$ phosphor does not have much effect on the bandgap.

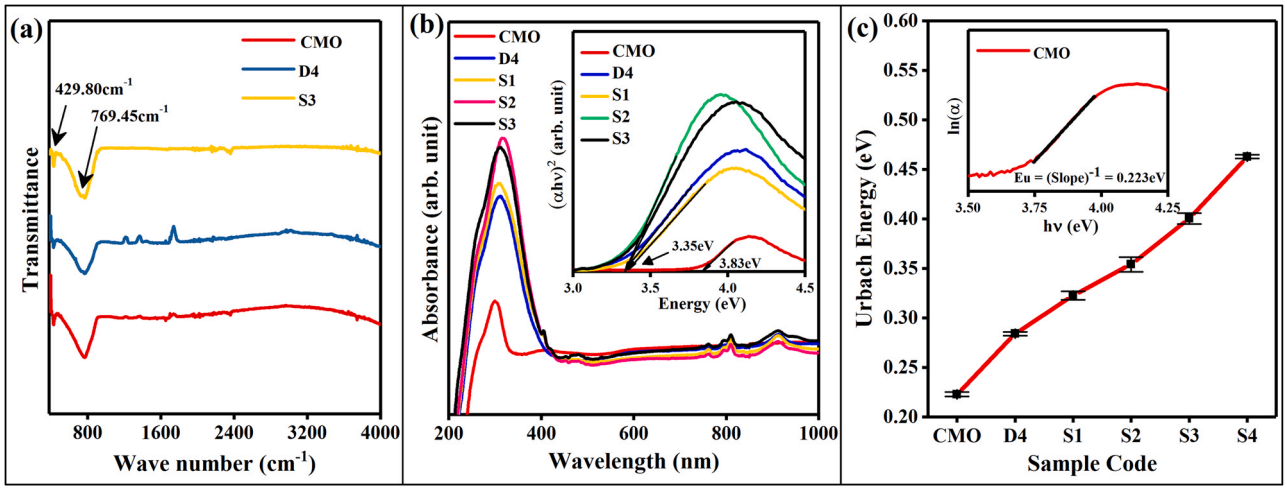

Fig. 5. (a) FTIR spectra of CMO, D4 and S3. (b) Absorption spectra and tauc plot (in inset) of CMO, D4, S1, S2, S3, and S4. (c) Urbach energy variation for CMO, D4, S1, S2, S3, and S4. Inset shows urbach energy plot of CMO.

The Urbach energy (E_u) gives the information about the creation of localized energy levels within the energy gap. The Urbach energy for the Sm^{3+} co-doped and Dy^{3+} doped samples can be evaluated via Urbach Empirical formula,

$$ln(\alpha) = \left(\frac{h\nu}{E_u}\right) + ln\beta$$

Where β is a constant, α is the absorption coefficient, $h\nu$ is the photon energy, and E_u represents the calculated Urbach energy [64]. For all the prepared samples, the inverse of the slope of $ln(\alpha)$ versus $h\nu$ plot gives the estimated Urbach energy (E_u), shown in Fig. 5(c). The $CaMoO_4$ has the minimum Urbach energy. The Urbach energy increases with Dy^{3+} doping in $CaMoO_4$ and Sm^{3+} co-doping in $CaMoO_4$:4 Dy^{3+}. The decrease in E_u validates the creation of defect levels in the energy gap. A similar tread in E_u for Dy^{3+}/Sm^{3+} doped phosphor is reported by Halimah et al. [65]. These defect levels depend on the concentration of dopant ions. It is responsible for the increase in the luminescence intensity by doping of activator ions [66].

3.6. Photoluminescence excitation (PLE) study

The comparative PLE spectrum of CMO, D2, D3, D4, and D5 are presented in Fig. 6(a), PLE spectrum of Sm2, Sm3, and Sm4 in Fig. 6(b), and the PLE spectrum of D4, S1, S2, S3, and S4 in Fig. 6(c). The PLE spectra of CMO is obtain for 500 nm emission wavelength. The broadband in the PLE spectrum of CMO centered at 296 nm is accredited to the ligands to metal charge transfer (LMCT) band, which is the result of charge transfer from filled 2p orbital of O^{2-} ion to the partially filled orbital of Mo^{6+} ion within the $[MoO4]^{-2}$ groups [60]. The PLE spectra of Sm series is obtained by monitoring $^4G_{5/2}\rightarrow{}^6H_{9/2}$ (646 nm) Sm^{3+} emission transition. The broadband shown in Fig. 6(b) is attributed to the overlap of LMCT band and charge transfer band (CTB). It is observed that for higher Sm^{3+} doping in $CaMoO_4$, the intensity of the broadband is increased and the broadband is also shifted to the higher wavelength. The shift and increase in the broadband is attributed to the overlap of the LMCT and CTB band [12]. Some f—f transitions of Sm^{3+} ion are also visible in the PLE spectrum, which is attributed to the energy transfer from the ground level $^6H_{5/2}$ to higher levels $^4L_{17/2}$ (367 nm), $^4K_{11/2}$ (378 nm), $^4F_{7/2}$ (407 nm), $^6P_{5/2}$ (422 nm), $^4I_{13/2,\ 11/2,\ 9/2}$ (465—483 nm) [12]. The PLE spectrum of D and S series were obtained by monitoring $^4F_{9/2}\rightarrow{}^5H_{13/2}$ (574 nm) Dy^{3+} emission transition. The broadband of excitation spectra centered at 296 nm have been recorded from 230 nm to 340 nm, which attributed to the overlap of LMCT band and CTB [67]. The CTB is due to charge transfer from filled 2p orbital of O^{2-} ion to the partially filled orbital of Dy^{3+} and Sm^{3+} ions. Some f—f transitions of Dy^{3+} ion are also visible in the PLE spectrum, which is attributed to the energy transfer from the ground level $^6H_{15/2}$ to higher levels $^6P_{3/2}$ (327 nm), $^6P_{7/2}$ (352 nm), $^6P_{5/2}$ (366 nm), $^4I_{13/2}$ (388 nm), $^4G_{11/2}$ (427 nm), $^4I_{15/2}$ (453 nm), and $^4F_{9/2}$ (476 nm). All observed excitation peaks of Dy^{3+}ion are in good agreement with the earlier reports [68].

The PLE intensity is increased on increasing the doping percentage of Dy^{3+} ions, and consequently D4 records the maximum intensity. After that, quenching is observed in the excitation spectrum, as shown in Fig. 6(a). The intensity the excitation peaks corresponding to Dy^{3+} ion decreases with an increase in the co-doping percentage of Sm^{3+} ions in D4 sample. The decrease in the excitation intensity is the result of energy transfer from Dy^{3+} ions to Sm^{3+} ions.

3.6.1. Photoluminescence emission (PL) study

The comparative PL spectra of CMO, D2, D3, D4, and D5 are depicted in Fig. 7(a), the PL spectra of Sm2, Sm3, and Sm4 in Fig. 7(b), and the PL spectra of D4, S1, S2, S3, and S4 in Fig. 7(c). The broadband in the PL spectra of CMO is centered at 500 nm which is because of the energy transfer from the conduction to valance band [67]. A variation in the intensity of broadband emission has been observed for Dy^{3+} doped phosphors, which indicates the effective charge transfer from CMO to Dy^{3+} ions. The broadband emission intensity is lowest for the D4 concentration, as shown in Fig. 7(a). Some sharp peaks corresponding to Dy^{3+} transitions are observed at 488 nm ($^4F_{9/2}\rightarrow{}^6H_{15/2}$) and 574 nm ($^4F_{9/2}\rightarrow{}^6H_{13/2}$) [69]. The $^4F_{9/2}\rightarrow{}^6H_{15/2}$ transition is the magnetic dipole transition, while the $^4F_{9/2}\rightarrow{}^6H_{13/2}$ transition is the electric dipole transition of Dy^{3+} ions, which is allowed at lower symmetries without an inversion center [68,69]. The chemical environment of Dy^{3+} ions realty affects the electric dipole transition, whereas the magnetic dipole transition is less sensitive to the chemical environment. Therefore, yellow emission (574 nm) is much intense compare to blue emission (488 nm) as shown in Fig. 7(a). The radius of the Dy^{3+} ion (91.2 pm) is comparable to the radius of the Ca^{2+} ion (100 pm), so Dy^{3+} ions can enter into low

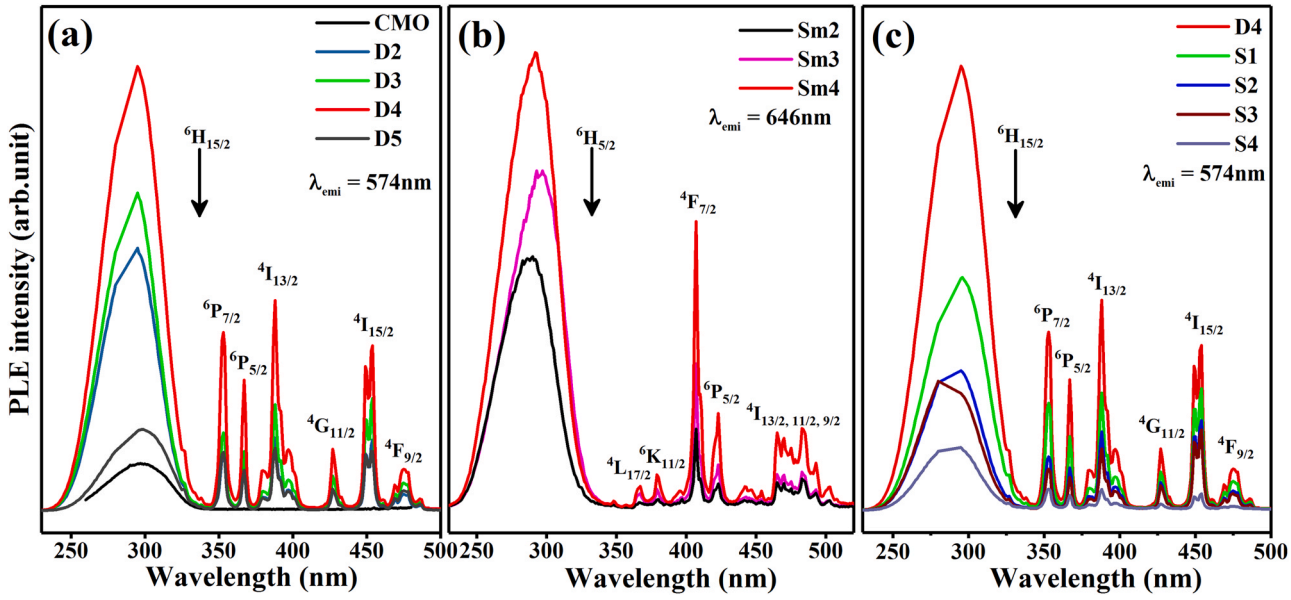

Fig. 6. Photoluminescence Excitation spectra of (a) Dy^{3+} doped $CaMoO_4$ phosphors and (b) Sm^{3+} doped $CaMoO_4$ phosphors (c) Sm^{3+} co-doped $CaMoO_4$:4Dy^{3+} phosphors.

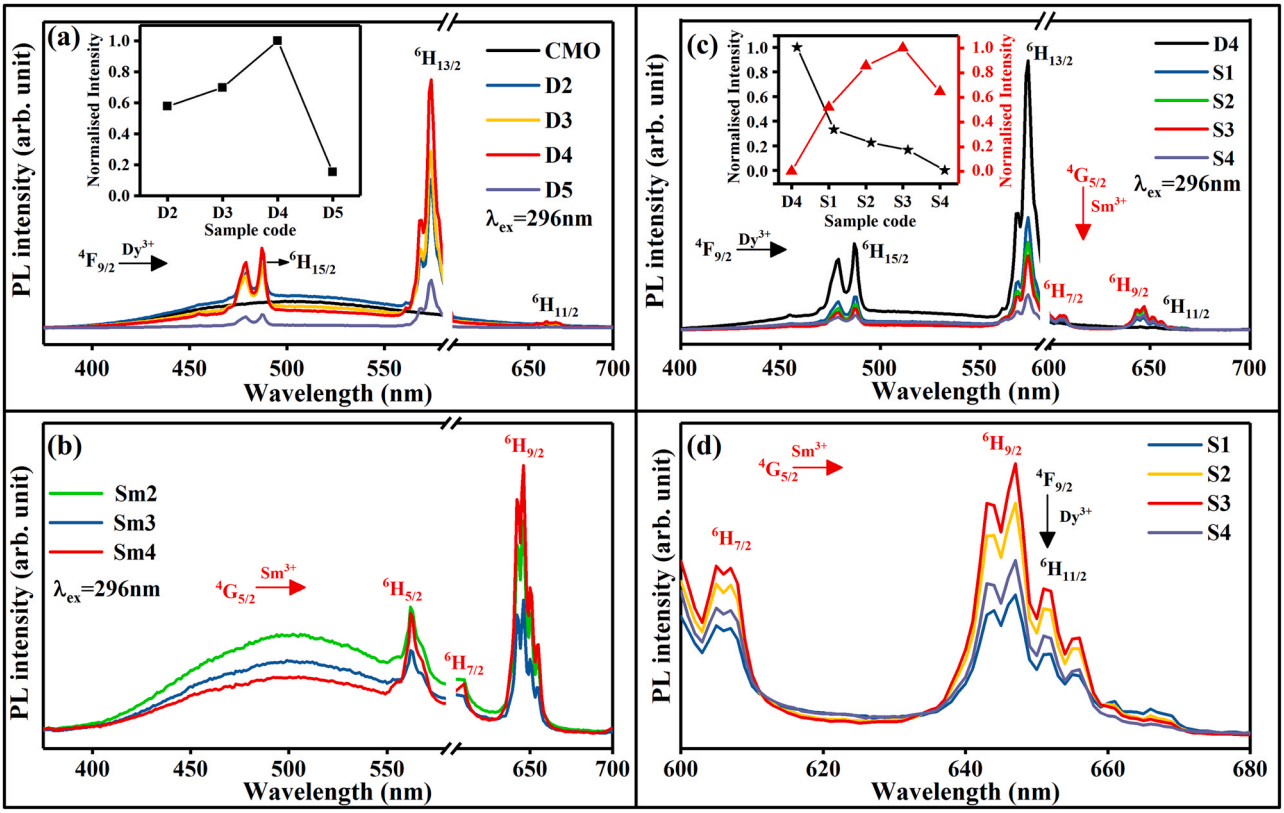

Fig. 7. PL spectra of (a) Dy^{3+} doped $CaMoO_4$ phosphors. Inset shows normalized PL intensity variation of 574 nm peak. (b) Sm^{3+} doped $CaMoO_4$ phosphors (c) Sm^{3+} co-doped $CaMoO_4$:4Dy^{3+} phosphors in range 400–700 nm. Inset shows normalized PL intensity variation of 574 nm (denoted by black line) and 646 nm peak (denoted by red line) (d) Sm^{3+} co-doped $CaMoO_4$:4Dy^{3+} phosphors in range 600–680 nm. (For interpretation of the references to colour in this figure legend, the reader is referred to the web version of this article.)

symmetry Ca^{2+} sites without an inversion center. Hence, we observe strong $^4F_{9/2}\rightarrow{}^6H_{13/2}$ electric dipole transition for Dy^{3+} doped phosphors. A weak band is also observed in the red region at 661 nm, which is due to the $^4F_{9/2}\rightarrow{}^6H_{11/2}$ transition. Some transition peaks are split into two or three emission peaks, which is due to the crystal field effect [70]. All emission transitions of Dy^{3+} ions are in good agreement with earlier reports [68]. Variation in 574 nm peak intensity with the Dy^{3+} doping concentration is plotted in the inset of Fig. 7(a). The PL intensity increases with increasing the doping percentage of Dy^{3+} and the maximum emission is observed D4 sample. After 4% concentration, we observe a quenching phenomenon which results in a decrease in emission intensity at higher Dy^{3+} concentration [71]. The PL spectra of Sm series in Fig. 7(b) shows a broadband centered at 500 nm which is attributed to the overlap of LMCT and CTB. Some characteristic peaks of Sm^{3+} ions which is attributed to the energy transfer from $^4G_{11/2}$ to lower levels $^6H_{5/2}$ (562 nm), $^6H_{7/2}$ (605 nm), $^6H_{9/2}$ (646 nm) are also observed in Fig. 7(b). It is observed that the emission intensity of the broadband decreases while the intensity of characteristic peaks increases, which is attributed to the energy transfer from CMO to Sm^{3+} ions.

This relative distance (d_r) between the emitting ions depends upon the critical concentration (c) of activator ion,volume of the unit cell (V), and the number of host cations per unit cell (N). And the relative distance (d_r) expression is written as below [72];

$$d_r = 1.24 * \sqrt[3]{\frac{V}{c * N}}$$

The unit cell volume (V) of the D4 sample is 312.169 Å^3, which is estimated from XRD analysis, critical concentration (c) of Dy^{3+} ion is 0.04, and the number of available lattice sites of $CaMoO_4$ in per unit cell (N) is 4. After calculation, the critical relative distance is 1.55 nm. Generally, quenching occurs either due to energy exchange or due to electrical multipolar transitions. The energy exchange occurs because of the overlap of the Dy^{3+}wave functions and the relative distance between Dy^{3+} ions must be less than 0.5 nm [73]. The calculated d_r indicates that the non-radiative energy transfer is not due to the overlap of the wave-functions of the Dy^{3+} ions but may be due to the electric multipolar interaction.

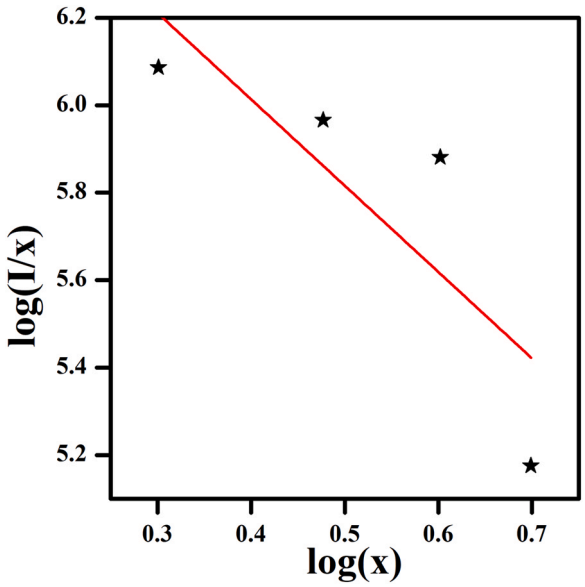

Fig. 8. Linear fitted curve of Dexter's expression for peak at 574 nm of 4% Dy^{3+} doped $CaMoO_4$.

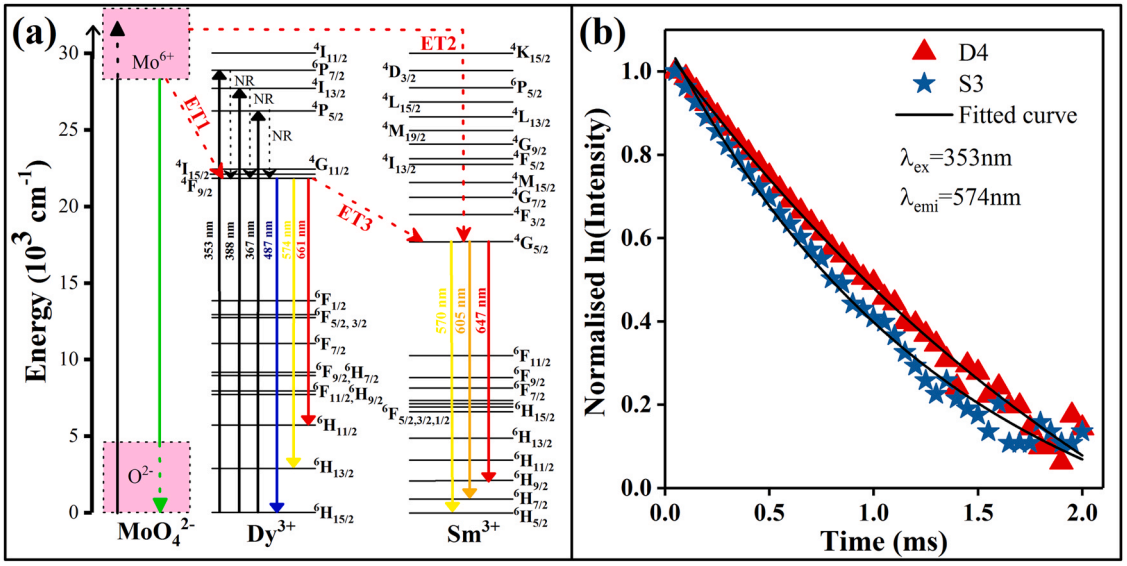

Fig. 9. (a) Energy level diagram showing energy transfer process. (b) Decay curves of D4 and S3 phosphors.

The form of multipolar interaction, which is responsible for quenching in $CaMoO_4$: x%Dy^{3+}, can determine by using the theory of Dexter. Dexter's expression can be converted in logarithm form, given by the following equation [74];

$$log\left(\frac{I}{x}\right) = C - \frac{Q}{3}log(x)$$

Where C is any constant, x (x = 2%, 3%, 4%, and 5%) is the percentage of Dy^{3+} doping concentration, and I denotes the intensity of transition peak correlated to Dy^{3+} doping percentage. The Q value gives the information of multipolar interaction, Q value represents dipole-dipole interaction, dipole-quadrupole interaction, and quadrupole-quadrupole interaction according to Q = 6, 8, and 10, respectively. The value of Q for 574 nm corresponding to Dy^{3+} emission transition $^4F_{9/2}\rightarrow{}^6H_{13/2}$ is thrice the negative slope of the plot $log(I/x)$ versus $log(x)$. The $log(I/x)$ versus $log(x)$ plot is depicted in Fig. 8. The value of Q for the yellow emission peak is 5.92, near around 6. Hence, the multipolar interaction is dipole-dipole interaction in Dy^{3+} doped $CaMoO_4$.

The energy transfer from Dy^{3+} to Sm^{3+} is realized by co-doping Sm^{3+} in the D4 phosphor. The PL spectra of Sm^{3+} co-doped $CaMoO_4$:4Dy^{3+} phosphors are presented in Fig. 7(c). Some other emission peaks around 605 nm and 646 nm are observed which corresponds to Sm^{3+} transition from $^4G_{5/2}$ to ^6H_j (j = 7/2, 9/2), respectively. The Sm^{3+} ion transition $^4G_{5/2}\rightarrow{}^6H_{7/2}$ (orange emission at 605 nm) is the magnetic dipole transition, and $^4G_{5/2}\rightarrow{}^6H_{9/2}$ transition (red emission at 647 nm) is the forced electric dipole transition [75]. The ionic radius of Sm^{3+} (108 pm) is comparable to the ionic radius of Ca^{2+} ion (100 pm), so the Sm^{3+} ions are placed easily in low symmetric sites of Ca^{2+} ions without an inversion symmetry similar to Dy^{3+} ions. All transition peaks of $Sm^{3+}$are in good agreement with the earlier reports [12]. Splitting of transition peaks occurs due to the crystal field effect. From Fig. 7(c) and Fig. 7(d), we infer that the emission intensity of the broadband and peaks corresponding to Dy^{3+} transition decreases, while the intensity of peaks corresponding to Sm^{3+} ions increases with the increase in co-doping concentration of Sm^{3+} ions. This variation in the intensities of the broadband and emission peaks corresponding to CMO, $Dy^{3+}$and Sm^{3+}ions manifest that energy transfer occurs from the CMO and Dy^{3+} ions to Sm^{3+} ions. The energy transfer occurs from the conduction band of $CaMoO_4$ to the intermediate excited levels of the Dy^{3+} and Sm^{3+} ions. Further, since the $^4G_{5/2}$ transition level of Sm^{3+} ions lies below Dy^{3+} transition levels, therefore energy transfer from Dy^{3+} to Sm^{3+} energy levels is prompted. The schematic of energy transfer process from the host to Dy^{3+}/Sm^{3+} ions and Dy^{3+} to Sm^{3+} energy levels is shown in the energy level diagram in Fig. 9(a). It is observed that the 3% Sm^{3+} co-doped phosphor has the maximum emission intensity, Fig. 7(c) and (d). On further increasing the doping percentage of Sm^{3+}, the intensity of Sm^{3+} emission transitions is quenched. The intensity variation of the strong emission of Dy^{3+} and Sm^{3+} ions in the Sm^{3+} co-doped D4 samples is shown in the inset of Fig. 7(c). Thus, energy is easily transferred from the host energy band to the Dy^{3+}/Sm^{3+} energy levels and from the Dy^{3+} energy levels to the Sm^{3+} energy levels. It is inferred that the Sm^{3+}/Dy^{3+} doped $CaMoO_4$ phosphor can produce white light by regulating the concentration of Dy^{3+} and Sm^{3+} ions. The prepared Sm^{3+}/Dy^{3+} doped $CaMoO_4$ phosphors can be used as a white light-emitting material in various optoelectronic devices, such as LEDs.

3.7. Decay curve analysis

The normalised PL decay curves of D4 and S3 phosphors in logarithmic scale for $^4F_{9/2}\rightarrow{}^6H_{13/2}$ transition (574 nm) upon 353 nm excitation are depicted in Fig. 9(b). We have examined the decay curves by fitting them with the biexponential equation [44]:

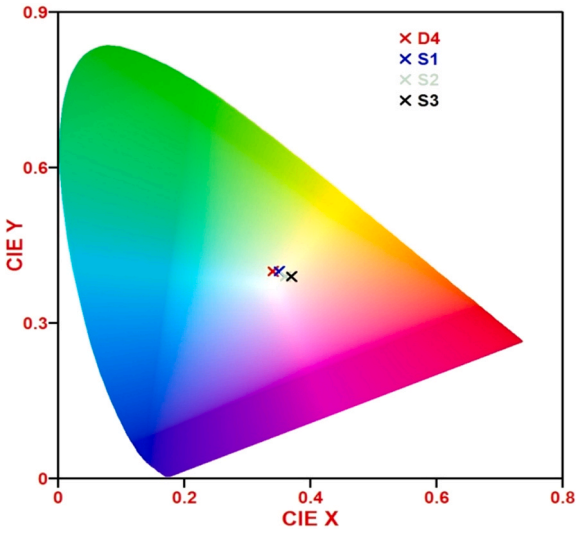

Fig. 10. Chromaticity diagram for D4, S1, S2, and S3.

Table 4
CIE coordinates, CCT value and color purity for D4, S1, S2, and S3.

Sample code name	CIE coordinate (x, y)	CCT (K)	Light Color	Color purity (%)
D4	(0.336, 0.397)	5389	Cold white light	19.1
S1	(0.345, 0.392)	5122	Cold white light	20.2
S2	(0.353, 0.387)	4867	Neutral white light	20.9
S3	(0.366, 0.380)	4439	Neutral white light	22.2

$$I(t) = I_0 + A_1\, exp\left(-\frac{t_1}{\tau_1}\right) + A_2\, exp\left(-\frac{t_2}{\tau_2}\right)$$

Where I_0 is the background intensity at a long time after excitation and I is the intensity after t seconds; fast and slow decay times are denoted by τ_1 and τ_2, respectively; A_1 and A_2 are the fitting constants. To calculate the average lifetime we have used the following relation [44]:

$$\tau_{avg} = (A_1\tau_1^2 + A_2\tau_2^2)/(A_1\tau_1 + A_2\tau_2)$$

Using equations (1) and (2), the average lifetime of $^4F_{9/2}$ level of the Dy^{3+} ion for D4 and S3 is 2.75 ms and 1.37 ms, respectively. It was observed that the lifetime of Dy^{3+} ions is decreased after 3% Sm^{3+} ions co-doping, which indicate the energy transfer process from Dy^{3+} to Sm^{3+} ions. The energy transfer efficiency (η_{ET}) can be calculated using the following relation

$$\eta_{ET} = 1 - \frac{\tau_x}{\tau_0}$$

Where τ_x and τ_0 are the average lifetime of $^4F_{9/2}$ level of the Dy^{3+} ion in S3 and D4 sample, respectively. The calculated η_{ET} is 50.1%, which is higher than many of the earlier reported phosphors with Dy^{3+} and Sm^{3+} co-doping [42,44]. The high value of η_{ET} support our analysis of energy transfer from Dy^{3+} to Sm^{3+} ions which we have discussed in previous section.

3.8. CIE, CCT and color purity study

The Commission Internationalede l'Elcairage (CIE) coordinates of D4, S1, S2, and S3 samples are calculated from their emission spectra and are labeled in the chromaticity diagram shown in Fig. 10 and the calculated CIE coordinate is tabulated in Table 4. The evaluated CIE coordinates for D4 are (0.3364, 0.3975), which lies in the near-white light region. For Sm^{3+} co-doped phosphor, CIE coordinates shift towards the red color region. The overall emission represents a white color with a combination of Dy^{3+} emission (blue & yellow peaks) and Sm^{3+} emission (red peak).

The correlated color temperature (*CCT*), which determines the calculated color temperature of the prepared phosphors used to concern quality of light can be calculated by using the given below equation [76];

$$\boldsymbol{CCT = -437n^3 + 3601n^2 - 6861n + 5514.31}$$

Where; $\boldsymbol{n = \frac{(x - x_e)}{(y - y_e)}}$ and the value of coordinate (x_e, y_e) is (0.33, 0.1858). The calculated *CCT* for 4% Dy^{3+} doped $CaMoO_4$ phosphor is 5389 K, which is in the cold white light region (> 5000 K). However, the calculated *CCT* of Sm^{3+} co-doped phosphor is 4439 K, which illustrates that emitting light color is moved from cold to neutral white light region. Similar observations have been also reported earlier by A. U. Trápala-Ramírez et al., E. F. Huerta et al. and H. I. Francisco-Rodriguez et al. [77-79]. The calculated *CCT* for all samples is listed in Table 4. It is inferred that the CIE coordinates and *CCT* value can be altered by regulating the Dy^{3+}/Sm^{3+} doping concentration in $CaMoO_4$ phosphor.

The color purity which represents the purity of monochromaticity of the overall emission is tabulated in Table 4. It is evaluated by the following expression [78,79]:

$$\boldsymbol{color\ purity}\ (\%) = \frac{\sqrt{(x_s - x_i)^2 + (y_s - y_i)^2}}{\sqrt{(x_d - x_i)^2 - (x_d - x_i)^2}} * 100$$

Where (x_s, y_s) are the coordinates of the prepared phosphor and (x_i, y_i) are the coordinates of white illumination point (0.3101, 0.3162) of the 1931 CIE Standard Source C. The (x_d, y_d) coordinates lie on the perimeter of the CIE diagram, which can be obtained by expanding the straight line between (x_i, y_i) and (x_s, y_s) up to the perimeter. The lower value of color purity percentage means that the overall emission of the phosphor is closer to white light. The calculated color purity percentage of all Sm^{3+} co-doped $CaMoO_4$:4Dy^{3+} phosphors is in the range 19%– 22% which is low, therefore it suggests that the overall emission of all phosphors is closer to white light.

4. Conclusion

In the present study we have successfully synthesized $CaMoO_4$, Dy^{3+}/Sm^{3+} doped $CaMoO_4$ and Sm^{3+} co-doped $CaMoO_4$:4Dy^{3+} phosphors via facile auto-combustion process. The structural analysis confirms the tetragonal crystal structure of $CaMoO_4$ and other doped phosphors. XPS analysis confirms the oxidation state of all the present elements in Sm^{3+}co-doped $CaMoO_4$:4Dy^{3+} phosphor. The PL spectrum depicts emission peaks of Dy^{3+} doped $CaMoO_4$ phosphors at 487 nm and 574 nm for near-UV light excitation (296 nm). After 4% Dy^{3+} concentration, quenching in emission intensity is observed which is due to dipole-dipole interaction between the Dy^{3+} ions in $CaMoO_4$. The shift from bluish white light to neutral white light is observed when Sm^{3+} ions are co-doped in $CaMoO_4$:4Dy^{3+} phosphor. The shift in the color of overall emission is attributed to the efficient energy transfer process from CMO to Dy^{3+}/Sm^{3+} ions and from Dy^{3+} to Sm^{3+} ions. The process of energy transfer is discussed in detail with the help of energy level diagram. The average lifetime of $^4F_{9/2}$ level of the Dy^{3+} ion is decreased with Sm^{3+} ion co-doping. The decreased average lifetime validates energy transfer from Dy^{3+} to Sm^{3+} ions and the calculated energy transfer efficiency is around 50% for S3 sample. It is observed that the Dy^{3+}/Sm^{3+} co-doped phosphors have low CCT value and low color purity percentage. Thus, the prepared Dy^{3+}/Sm^{3+} co-doped $CaMoO_4$ phosphor can be a good alternative for various optoelectronic applications.

CRediT authorship contribution statement

Prashant Dixit: Conceptualization, Investigation, Formal analysis, Visualization, Writing – original draft. **Vaibhav Chauhan:** Writing – original draft, Writing – review & editing. **S. B. Rai:** Resources. **Praveen C. Pandey:** Resources, Writing – review & editing, Supervision, Validation.

Declaration of Competing Interest

The authors declare that they have no known competing financial interests or personal relationships that could have appeared to influence the work reported in this paper.

Acknowledgments

Prashant Dixit and Vaibhav Chauhan are thankful to UGC, India, and CSIR, India for the financial support provided in the form of a senior research fellowship. Authors are thankful to DST-FIST for providing UV–Vis spectrophotometer, FTIR spectrometer.

References

[1] S. Sharma, S. Pitale, M. Malik, M. Qureshi, R. Dubey, Spectral and kinetic characterization of orange-red emitting $Sr_3Al_2O_6:Eu^{3+}/Sm^{3+}$ phosphor, J. Alloys Compd 482 (2015), pp. 468–475.

[2] C. Wei, D. Xu, Z. Yang, J. Li, X. Chen, X. Li, J. Sun, Insight into the synthesis and luminescence properties of the single-ion-activated single-phased $Na_3ScSi_2O_7:Dy^{3+}$ phosphor for white light-emitting diodes, Appl. Phys. A. 125 (2019) 1–6.

[3] F. Xie, J. Li, Z. Dong, D. Wen, J. Shi, J. Yan, M. Wu, Energy transfer and luminescent properties of $Ca_8MgLu(PO_4)_7:Tb^{3+}/Eu^{3+}$ as a green-to-red color tunable phosphor under NUV excitation, RSC Adv. 5 (2015) 59830–59836.

[4] Ilknur Kars Durukan, Mustafa Kemal, €Oztürk, Süleyman €Ozçelik, Ekmel €Ozbay, Analyzing the InGaN LED structures for white LED applications, J. Polytech. 20 (2017) 531–536.

[5] S. Nishiura, S. Tanabe, K. Fujioka, Y. Fujimoto, Properties of transparent Ce^{3+}: YAG ceramic phosphors for white LED, Opt. Mater. 33 (2011) 688–691.

[6] Samuel Petera, Aum Patela, Kitai Adrian, Photoluminescence enhancement of Ce^{3+}: YAG nanophosphors via doped/intrinsic core/shell structures, J. Lumin. 211 (2019) 82–87.

[7] Qinyu Li, Lan Yu, Weiping Wu, Chang Liu, Mengjiao Liu, Ling Huang, Yan Zhao, Xin Lai, Jian Bi, Daojiang Gao, Novel $BaGe_{1-x}Si_xF_6$: Mn^{4+} ($0 \le x \le 1$) red phosphors for warm white LEDs: Hydrothermal synthesis and photoluminescence properties, J. Alloy. Compd. 852 (2021) 156995.

[8] Lili Wang, Byung Kee Moon, Sung Heum Park, Jung Hwan Kim, Jinsheng Shi, Kwang Ho Kim, Jung Hyun Jeong, Photoluminescence properties, crystal structure and electronic structure of a $Sr_2CaWO_6:Sm^{3+}$ red phosphor, RSC Adv. 5 (2015) 89290–89298.

[9] W. Zhang, G. Yan, S. Dai, P. Zhang, Q. Zhao, K. Qiu, M. Deng, Effects of charge compensator Li^+ co-doping on the structure and luminescence properties of $Cd_2V_2O_7:Eu^{3+}$ red phosphors, Ceram. Int 44 (2018), pp. 9534–9539.

[10] Z. Jia, X. Zhang, X. Hua, Y. Dong, H. Li, C. Feng, Y. Wang, M. Xia, Engineering mixed polyanion red-emitting $Rb_2Bi(PO_4)(WO_4):Eu^{3+}$ phosphors with negligible thermal quenching and high quantum yield, J. Alloys Compd 844 (2020).

[11] S. You, Y. Zhuo, Q. Chen, J. Brgoch, R.-J. Xie, Dual-site occupancy induced broadband cyan emission in $Ba_2CaB_2Si_4O_{14}:Ce^{3+}$, J. Mater. Chem. C. 8 (2020) 15626–15633.

[12] Vaibhav Chauhan, Prashant Dixit, Praveen C. Pandey, Bi^{3+} assisted luminescence in $SrMoO_4:Sm^{3+}$ red phosphors, J. Rare Earths. 39 (11) (2021) 1336–1343.

[13] J. Hou, X. Yin, F. Huang, W. Jiang, Synthesis and photoluminescence properties of $NaLaMgWO_6:RE^{3+}$ (RE = Eu, Sm, Tb) phosphor for white LED application, Mater. Res. Bull. 47 (2012) 1295–1300.

[14] Ying Li, Zhongxian Qiu, Jilin Zhang, Xiaoyu Ji, Xinguo Zhang, Shuzhen Liao, Wenli Zhou, Liping Yu, Shixun Lian, Highly efficient and thermally stable single-activator white-emitting phosphor $K_2Ca(PO_4)F:Eu^{2+}$ for white light-emitting diodes, J. Mater. Chem. C 7 (2019), pp. 8982–8991.

[15] Jin-jun Cai, Huan-huan Pan, Yi Wang, Synthesis and luminescence properties of Ca_2SiO_4-based red phosphors with Sm^{3+} doping for white LEDs, Int. J. Miner. Metall. 19 (2012) 663–667.

[16] P. Babu, Kyoung Hyuk Jang, Ch. Srinivasa Rao, Liang Shi, C.K. Jayasankar, Víctor Lavín, and Hyo Jin Seo, White light generation in Dy^{3+}-doped oxyfluoride glass and transparent glass-ceramics containing CaF_2 nanocrystals, Opt. Express 19 (3) (2011) 1836–1841.

[17] B.P. Maheshwary, R.A. Singh, Singh, Effect of annealing on the structural, optical and emissive properties of $SrWO_4:Ln^{3+}$ (Dy^{3+}, Eu^{3+} and Sm^{3+}) nanoparticles, Spectrochim. Acta A Mol. Biomol. 152 (2016) 199–207.

[18] Nameeta Shweta Sharma, D.P. Brahme, Bisen, Pradeep Dewangan, Cool white light emission from Dy^{3+} activated alkaline alumino silicate phosphors, Opt. Express 26 (22) (2018) 29495–29508.

[19] Chao Xu, Dingbing Zou, Hai Guo, Jie Feng, Taokai Ying, Luminescence properties of hierarchical $CaMoO_4$ microspheres derived by ionic liquid-assisted process, J. Lumin. 129 (2009) 474–477.

[20] Prashant Dixit, Vaibhav Chauhan, Pawan Kumar, Praveen C. Pandey, Enhanced photoluminescence in $CaMoO_4:Eu^{3+}$ by Mn^{2+} co-doping, J. Lumin 223 (2020).

[21] Chanchal Hazra, Tuhin Samanta, Aswin Vijai Asaithambi, Venkataramanan Mahalingam, Bilayer stabilized Ln^{3+}-doped $CaMoO_4$ nanocrystals with high luminescence quantum efficiency and photocatalytic properties, Dalton Trans. 43 (2014) 6623-30.

[22] Li Han, Guixia Liu, Xiangting Dong, Jinxian Wang, Xinlu Wang, Ying Yang, A potential single-component white-light-emitting phosphor $CaMoO_4:La^{3+},Dy^{3+}$: hydrothermal synthesis, luminescence properties and energy transfer, J. Mater. Sci: Mater. Electron 28 (2017) 16519–16526.

[23] L.B. Barbosaa, D. Reyes Ardilaa, C. Cusatisb, J.P. Andreeta, Growth and characterization of crack-free scheelite calcium molybdate single crystal fiber, J. Cryst. Growth 235 (2002) 327–332.

[24] X. Zhang, J. Lin, V.B. Mikhailik, H. Kraus, Studies of scintillation properties of $CaMoO_4$ at millikelvin temperatures, Appl. Phys. Lett. 106 (2015) 241904.

[25] Geun-Kyu Choi, Seo-Yong Cho, Jae-Sul An, Kug Sun Hong, Microwave dielectric properties and sintering behaviors of scheelite compound $CaMoO_4$, J. Eur. Ceram. Soc. 26 (2006) 2011–2015.

[26] Hom Nath Luitel, Rumi Chand, Toshio Torikai, Mitsunori Yadaa, Takanori Watari, Highly efficient NIR–NIR upconversion in potassium substituted $CaMoO_4:Tm^{3+}$, Yb^{3+} phosphor for potential biomedical applications, RSC Adv. 5 (2015) 17034–17040.

[27] Jeong Ho Ryu, Bong Geun Choi, Jong-Won Yoon, Kwang Bo Shim, Kinuyo Machi, Kenji Hamada, Synthesis of $CaMoO_4$ nanoparticles by pulsed laser ablation in deionized water and optical properties, J. Lumin. 124 (2007) 67–70.

[28] Abdul Kareem Parchur, Raghumani Singh Ningthoujam, Shyam Bahadur Rai, Gunadhor Singh Okram, Ram Asaray Singh, Mohit Tyagi, S.C. Gadkari, Raghvendra Tewari, Rajesh Kumar Vatsa, Luminescence properties of Eu^{3+} doped $CaMoO_4$ nanoparticles, Dalton Trans. 40 (2011) 7595-601.

[29] Jai Bhagwan, Sk. Khaja Hussain, Jae Su Yu, Facile hydrothermal synthesis and electrochemical properties of $CaMoO_4$ nanoparticles for aqueous asymmetric super capacitors, ACS Sustain, Chem. Eng. 7 (2019) 12340–12350.

[30] G. Botelho, I.C. Nogueira, E. Moraes, E. Longo, Study of structural and optical properties of $CaMoO_4$ nanoparticles synthesized by the microwave-assisted solvothermal method, Mater. Chem. Phys. 183 (2016) 110–120.

[31] Jun Wang, Feng Cai-Ting, Yu Hai-Hui, Green synthesis of nanoparticles molybdate doped with rare earth ion and its luminescence property, Adv, J. Food Sci. Technol. 9 (7) (2015) 519–522.

[32] Haoyi Wu, Yihua Hu, Wei Zhang, Fengwen Kang, Nana Li, Guifang Ju, Sol–gel synthesis of Eu^{3+} incorporated $CaMoO_4$: the enhanced luminescence performance, J. Sol. Gel Sci. Technol. 62 (2012) 227–233.

[33] E. Sinha, P. Yadav, Study of structural and optical properties of $CaMoO_4$ ceramic synthesized by solid state reaction route, Ferroelectrics 517 (2017) 1–7.

[34] C.R.R. Almeida, L.X. Lovisa, A.A.G. Santiago, M.S. Li, E. Longo, C.A. Paskocimas, F.V. Motta, M.R.D. Bomio, One-step synthesis of $CaMoO_4:Eu^{3+}$nanospheres by ultrasonic spray pyrolysis, J. Mater. Sci. Mater. Electron 28 (2017), pp. 16867–16879.

[35] X. Xiao, B. Yan, Chemical co-precipitation synthesis and photoluminescence of Eu^{3+} or Dy^{3+} doped $Zn_3Nb_2O_8$ microcrystalline phosphors from hybrid precursors, Mater. Sci. Eng. B 136 (2007) 154–158.

[36] R.S. Yadav, R.K. Dutta, M. Kumar, A.C. Pandey, Improved color purity in nano-size Eu^{3+}-doped YBO_3 red phosphor, J. Lumin. 129 (2009) 1078–1082.

[37] Enrico Cavalli, Enrico Bovero, Alessandro Belletti, Optical spectroscopy of $CaMoO_4:Dy^{3+}$ single crystals, J. Phys.: Condens. Matter 14 (2002) 5221–5228.

[38] Guan Li, Jia Guoqi, Yang Baozhu, Li Xu, Jin Litao, Yang Zhiping, Fu Guangsheng, Synthesis and optical properties of Dy^{3+}, Li^+ doped $CaMoO_4$ phosphor, J. Rare Earths. 29 (2011) 540–543.

[39] G. Zhu, Z.-W. Li, C. Wang, F.-G. Zhou, Y. Wen, S.-Y. Xin, Electronic structure and photoluminescence property of a novel white emission phosphor $Na_3MgZr(PO_4)_3:Dy^{3+}$for warm white light emitting diodes, Chin. Phys. B 26 (2017) 097801.

[40] B. Han, H. Liang, H. Lin, W. Chen, Q. Su, G. Yang, G. Zhang, Enhanced luminescence of $Ba_3La(PO_4)_3:Dy^{3+}$ by co doping Gd^{3+} ions and energy transfer between Gd^{3+} and Dy^{3+}, J. Opt. Soc. Am. B 25 (2008) 2057–2063.

[41] Q. Liu, Y. Liu, Y. Ding, Z. Peng, X. Tian, Q. Yu, G. Dong, A white light emitting luminescent material $Ba_3Y(PO_4)_3:Dy^{3+}$, Ceram. Int. 40 (2014) 10125–10129.

[42] Bin Fan, Jun Liu, Wenyu Zhao, Limin Han, Luminescence properties of Sm^{3+} and Dy^{3+} co-doped BaY_2ZnO_5 phosphor for white LED, J. Lumin. 219 (2020) 116887.

[43] Ning Liu, Lefu Mei, Libing Liao, Jie Fu, Dan Yang, High Thermal Stability Apatite Phosphors $Ca_2La_8(SiO_4)_6O_2:Dy^{3+}/Sm^{3+}$ for White Light Emission: Synthesis, Structure, Luminescence Properties and Energy Transfer, Sci. Rep. 9 (2019) 15509.

[44] Feng Xu, Xiong Zhou, Haiping Xia, Hongwei Song, Baojiu Chen, Highly thermally stable Dy^{3+}/Sm^{3+} co-doped $Na_5Y_9F_{32}$ single crystals for warm white LED, J. Phys. Chem. Solids 158 (2021) 110240.

[45] Wen Yan, Junhan Li, Wentao between rare earth ions, Mater. Sci: Mater. Electron. 32 (2021) 16648–16661 Zhang, Xi Gao, and Peicong Zhang, Warm-white luminescence of Dy^{3+} and Sm^{3+} co-doped $NaSrPO_4$ phosphors through energy transfer.

[46] F.K.F. Oliveira, M.C. Oliveira, L. Gracia, R.L. Tranquilin, C.A. Paskocimas, F.V. Motta, E. Longo, J. Andres, M.R.D. Bomio, Experimental and theoretical study to explain the morphology of $CaMoO_4$ crystals, J. Phys. Chem. Solid. 114 (2018) 141–152.

[47] S.N. Achary, S.J. Patwe, M.D. Mathews, A.K. Tyagi, High temperature crystal chemistry and thermal expansion of synthetic powellite ($CaMoO_4$): A high temperature X-ray diffraction (HT-XRD) study, J. Phys. Chem. Solids 67 (2006) 774–781.

[48] R.D. Shannon, Revised effective ionic radii and systematic studies of interatomic distances in halides and chaleogenides, ActaCrystallogr 32 (1976) 751.

[49] J. Rodriguez- Carvajal. FULLPROF, a Rietveld and pattern matching analysis program. Laboratoire Leon Brillouin (CEA-CRNS), Paris, France.

[50] V. Mote, Y. Purushotham, B. Dole, Williamson-Hall analysis in estimation of lattice strain in nanometer-sized ZnO particles, J. Theor. Appl. Phys. 6 (2012) 6.

[51] M. Upasani, Synthesis of $Y_3Al_5O_{12}:Eu^{3+}$ and $Y_3Al_5O_{12}:Eu^{3+}$, Si phosphors by combustion method: Comparative investigations on the structural and spectral properties, J. Adv. Ceram. 5 (2016) 344–355.

[52] A. Maurya, R.S. Yadav, R.V. Yadav, S.B. Rai, A. Bahadur, Enhanced green upconversion photoluminescence from Ho^{3+}/Yb^{3+} co-doped $CaZrO_3$ phosphor via Mg^{2+} doping, RSC Adv. 6 (2016) 113469–113477.

[53] Santosh K. Gupta, M. Sahu, P.S. Ghosh, Deepak Tyagi, M.K. Saxena, R.M. Kadama, Energy transfer dynamics and luminescence properties of Eu^{3+} in $CaMoO_4$ and $SrMoO_4$, Dalton Trans. 44 (2015) 18957-69.

[54] B.P. Singh, A.K. Parchur, R.S. Ningthoujam, A.A. Ansari, P. Singh, S.B. Rai, Influence of Gd^{3+} co-doping on structural property of $CaMoO_4$:Eu^{3+} nanoparticles, Dalton Trans 43 (2014), p. 4770.
[55] P. Gupta, A.K. Bedyal, V. Kumar, Y. Khajuria, V. Kumar, E. Coetsee-hugo, O.M. Ntwaeaborwa, H.C. Swart, Spectral and surface investigations on Eu^{3+} doped $K_3Y(PO_4)_2$ nanophosphor: A promising orange-red phosphor for white light-emitting diodes, Opt. Mater. (Amst.). 36 (2014) 996–1001.
[56] K. Munirathnam, P.C. Nagajyothi, D. Prakashbabu, B.D.P. Raju, J. Shim, X-ray photoelectron spectroscopy and optical analysis of pure white light emitting Dy^{3+} and Mn^{2+}codoped Na_3Y $(PO_4)_2$ phosphors for solid-state lighting, Ceram. Int. 45 (2019) 686–694.
[57] K. Munirathnam, Ramaraghavulu Rajavaram, P.C. Nagajyothi, S. Thiyagaraj, M. Srinivas, Synthesis and optimization of Dy^{3+}-doped $SrZr_4(PO_4)_6$ nanophosphors for plant growth light-emitting diodes, Solid State Sci. 109 (2020) 106455.
[58] Peijing Tiana, Jinshu Cheng, Gaoke Zhang, X-ray photoelectron spectroscopy of Sm^{3+}-doped CaO–MgO–Al_2O_3–SiO_2 glasses and glass ceramics, Appl. Surf. Sci. 257 (2011) 4896–4900.
[59] D.L. Rousseau, R.P. Bauman, S.P.S. Porto, Normal mode determination in crystals, J. Raman Spectrosc. 10 (1981) 253–290.
[60] Z.F. Yao, G.H. Zheng, Z.X. Dai, L.Y. Zhang, Synthesis of the Dy^{3+}: $SrMoO_4$ with High Photocatalytic Activity under Visible Light Irradiation, Appl. Organo Met. Chem. 32 (2018) 4412.
[61] P. Suthanthirakumar, K. Marimuthu, Investigations on Spectroscopic properties of Dy^{3+} doped Zinc telluro-fluoroborate glasses for Laser and White LED applications, J. Mol. Struct. 1125 (2016) 443–452.
[62] K. Venkata Raoa, S. Babub, K.V. Subba Reddya, S. Subbarayudua, Y.C. Ratnakaramb, Optical Absorption and Luminescence Properties of Sm^{3+} Doped Chlorofluoro Borate Glasses for Photonic Applications, Int. J. Cur. Res. Rev. 9 (2017).
[63] S. Dutta, S. Som, S.K. Sharma, Luminescence and photometric characterization of K^+ compensated $CaMoO_4$:Dy^{3+} nanophosphors, Dalton Trans. 42 (2013) 9654–9661.
[64] S. Jana, A. Mondal, J. Manam, S. Das, Pr^{3+} doped $BaNb_2O_6$ reddish orange emitting phosphor for solid state lighting and optical thermometry applications, J. Alloy. Compd. 821 (2020) 153342.
[65] M.K. Halimah, M.F. Faznny, M.N. Azlan, H.A.A. Sidek, Optical basicity and electronic polarizability of zinc borotellurite glass 4 doped La^{3+} ions, Results Phys. 7 (2017) 581–589.
[66] Wasanthamala Badalawa, Hiroaki Matsui, Takamasa Osone, Noriyuki Hasuike, Hiroshi Harima, Hitoshi Tabata, Correlation between structural and luminescent properties of Eu^{3+}-doped ZnO epitaxial layers, J. Appl. Phys. 109 (2011) 053502.
[67] L. Krishna Bharat, G. Seeta Rama Raju, Jae Su Yu, Red and green colors emitting spherical-shaped calcium molybdate nanophosphors for enhanced latent fingerprint detection, Sci. Rep. 7 (2017) 11571.
[68] Puneet Kaur, Atul Khanna, M.N. Singh, A.K. Sinha, Structural and optical characterization of Eu^{3+} and Dy^{3+} doped $CaWO_4$ nanoparticles for white light emission, J. Alloy. Compd. 834 (2020) 154804.
[69] Z. Hu, T. Meng, W. Zhang, D. Ye, Y. Cui, L. Luo, Y. Wang, Synthesis and luminescence of Dy^{3+}-activated $NaSrPO_4$ phosphors for novel white light generation, J. Mater. Sci. -Mater. Electron 25 (2014) 1933–1937.
[70] J.X. Wu, M. Li, H.L. Jia, M.T. Wang, Z.G. Liu, Influences of calcinations temperature and charge compensators on the properties of $SrMoO_4$: Sm^{3+} red phosphor prepared via the sol–gel method, J. Lumin. 214 (2019) 116607.
[71] Weiguang Ran, Hyeon Mi Noh, Sung Heum Park, Byung Kee Moon, Jung Hyun Jeong, Jung Hwan Kim, Jinsheng Shi, Break the interacting bridge between Eu^{3+} ions in the 3D network structure of $CdMoO_4$: Eu^{3+} bright red emission phosphor, Sci. Rep. 8 (2018) 5936.
[72] G. Blasse, Energy transfer in oxidic phosphors, Phys. Lett. A 28 (1968) 444–445.
[73] B. Han, J. Zhang, Z.M. Wang, Y.Y. Liu, H.Z. Shi, Investigation on the concentration quenching and energy transfer of red-light-emitting phosphor Y_2MoO_6:Eu^3, J. Lumin 149 (2014), pp. 150–154.
[74] B. Devakumar, P. Halappa, C. Shivakumara, Dy^{3+}/Eu^{3+} co-doped $CsGd(MoO_4)_2$ phosphor with tunable photoluminescence properties for near-UV WLEDs applications, Dyes Pigm 137 (2016) 244–255.
[75] Shidong Li, Qingyu Meng, Shuchen Lü, Wenjun Sun, Optical properties of Sm^{3+} and Tb^3+ co-doped $CaMoO_4$ phosphor for temperature sensing, Spectrochim. Acta A Mol. Biomol. 214 (2019) 537–543.
[76] J. An, Z. Zhang, Y. Qiu, Z. Fu, Y. Zhou, F. Zeng, Luminescence properties of borosilicate glass doped with Ce^{3+}/Dy^{3+}/Eu^{3+} under ultraviolet excitation for white LED, J. Non-Cryst. Solids 503– 504 (2019) 208–213.
[77] H.I. Francisco-Rodriguez, A. Lira, O. Soriano-Romero, A.N. Meza Rocha, S. Bordignon, A. Speghini, R. Lozada-Morales, U. Caldiño, Lithium-aluminum-zinc phosphate glasses activated with Tb^{3+} and Tb^{3+}/Eu^{3+} for green laser medium, reddish-orange and white phosphor applications, Opt. Mater. 79 (2018) 358–365.
[78] E.F. Huerta, O. Soriano-Romero, A.N. Meza-Rocha, S. Bordignon, A. Speghini, U. Caldiño, Lithium-aluminum-zinc phosphate glasses activated with Sm^{3+}, Sm^{3+}/Eu^{3+} and Sm^{3+}/Tb^{3+} for reddish-orange and white light generation, J. Alloy. Compd. 846 (2020) 156332.
[79] A.U. Trápala-Ramírez, J.L.N. Gálvez-Sandoval, A. Lira, I. Camarillo, E. Alvarez Ramos, A.N. Meza-Rocha, U. Caldiño, Calcium-zinc phosphate glasses activated with Tb^{3+}/Eu^{3+} for laser and white LED applications, J. Lumin. 215 (2019) 116621.